A shock-stable modification of the HLLC Riemann solver with reduced numerical dissipation

Nico Fleischmann *, Stefan Adami, Nikolaus A. Adams

Technical University of Munich, Department of Mechanical Engineering, Chair of Aerodynamics and Fluid Mechanics, Boltzmannstraße 15, 85748 Garching, Germany

A R T I C L E   I N F O

A B S T R A C T

The purpose of this paper is twofold. First, the application of high-order methods in combination with the popular HLLC Riemann solver demonstrates that the grid-aligned shock instability can strongly affect simulation results when the grid resolution is increased. Beyond the well-documented two-dimensional behavior, the problem is particularly troublesome with three-dimensional simulations. Hence, there is a need for shock-stable modifications of HLLC-type solvers for high-speed flow simulations.

Second, the paper provides a stabilization of the popular HLLC flux based on a recently proposed mechanism for grid aligned-shock instabilities Fleischmann et al. (2020) [8]. The instability was found to be triggered by an inappropriate scaling of acoustic and advection dissipation for local low Mach numbers. These low Mach numbers occur during the calculation of fluxes in transverse direction of the shock propagation, where the local velocity component vanishes. A centralized formulation of the HLLC flux is provided for this purpose, which allows for a simple reduction of nonlinear signal speeds. In contrast to other shock-stable versions of the HLLC flux, the resulting HLLC-LM flux *reduces the inherent numerical dissipation* of the scheme.

The robustness of the proposed scheme is tested for a comprehensive range of cases involving strong shock waves. Three-dimensional single- and multi-component simulations are performed with high-order methods to demonstrate that the HLLC-LM flux also copes with latest challenges of compressible high-speed computational fluid dynamics.

1. Introduction

Approximate Riemann solvers in combination with shock-capturing Godunov schemes [1] dominate modern computation of phenomena that involve complex flow interactions across scales such as shock interaction with multi-phase interfaces and turbulent scales. The application of high-order discretizations allows for an accurate prediction of many of such flows. However, over the last decades the grid-aligned shock instability has presented a barrier for robust computation of high Mach number flows using high-order discretizations with state-of-the-art low-dissipation Riemann solvers such as Roe [2] or HLLC [3,4]. Since the first description of the problem by Peery and Imlay [5] and Quirk [6] an extensive research on the topic resulted in a large number of scientific publications addressing various aspects. A summary of major developments to

the present day can be found in [7,8]. Even though most of the research has focused on the Roe solver, also the HLLC solver is afflicted by the instability.

HLL-type solvers were originally developed by Harten, Lax and van Leer [3]. In combination with the nonlinear signal speed estimates of Einfeldt [9] and the restoration of the contact wave proposed by Toro et al. [4], the resulting HLLC Riemann approximation became one of the most successful and widespread Riemann solvers for hyperbolic systems [10,11]. An accurate estimation of the contact wave speed was communicated by Batten et al. [12]. Due to the explicit modeling of each wave of the governing Euler equations, HLLC is a complete Riemann solver with significantly reduced dissipation near contact discontinuities compared to the HLL scheme. The design of the HLLC flux allows for straightforward extensions to other types of hyperbolic equations, e.g. for magneto-hydrodynamics [13–15], by introduction of additional wave types. Moreover, the HLLC flux has been applied successfully to multi-component flows [16,17], and capillary forces have been introduced to simulate surface tension effects at liquid/gas interfaces [18]. Further recent applications are reviewed in [11].

While the HLLC flux is known to suffer from the shock instability, the stable behavior of the HLL flux was described already by Quirk [6]. He suggested to apply the HLL scheme near strong shocks in combination with lower-dissipation schemes, such as HLLC, in the remaining domain. These hybrid schemes lead to stable, but nevertheless contact preserving results. The switching procedure was improved by Kim et al. [19], where the dissipative HLL flux only is applied for the fluxes in transverse direction of the shock propagation. Another modification of the hybrid scheme was suggested in [20], where the dissipative HLL flux only is applied for two components of the flux. However, hybrid schemes may still significantly increase dissipation, and a switching procedure has to be provided. Additionally, the authors of [20] successfully tested the shock stability of the rotated Riemann solver method [21] applied to the HLLC flux, but they found that the latter approach is computationally rather expensive. The first pure HLLC-type flux with shock-stable properties, called HLLCM, was developed by Shen et al. [22] via smearing of the shear velocities on both sides of the contact line. This procedure introduces shear viscosity and stabilizes the calculation of strong shocks. However, the introduced amount of dissipation limits the accuracy of boundary layer calculations and therefore the authors again suggested to apply a hybrid HLLC-HLLCM version for complex flows. Recently, Xie et al. [23] proposed an HLLC-type Riemann solver with an additional pressure-dissipation term that is activated near shocks and damps spurious pressure perturbations. Simon and Mandal [24,25] proposed two different approaches to avoid the shock instability. They separated the HLLC flux into the inherent HLL part and an antidiffusive part. In their first approach [24], the activation of the antidiffusive term is controlled by a pressure-ratio-based multi-dimensional shock sensor. The resulting solver called HLLC-ADC restores the shock stability of the HLL flux. The second approach [25] is to apply a selective wave modification that increases the inherent dissipative HLL part in the vicinity of a shock wave. The antidiffusive term of the resulting HLLC-SWM flux remains identical to that of the original HLLC.

In comparison to the large number of proposed modifications of the Roe flux, the grid-aligned shock instability of the popular HLLC solver has found much less consideration in literature. The reason is probably, that the solution of most two-dimensional simulations remains bounded, and therefore the effect of the introduced disturbances is not as catastrophic as with the Roe flux. However, with increased resolution, high-order discretizations, and extension to three-dimensional simulations, the application of the HLLC flux is prone to develop severe carbuncles, similarly to that obtained with the Roe flux, as is shown in this paper.

In [8], the authors proposed a new possible mechanism of the grid-aligned shock instability. A wrong scaling behavior of numerical dissipation due to the local low Mach number in transverse direction of the shock front propagation was found to cause the numerical shock instability. A modification for the popular Roe flux and the local componentwise Lax-Friedrichs flux was proposed that proved to be shock stable. The present paper proposes a new shock-stable modification of the HLLC flux called HLLC-LM that is based on these findings. As a straightforward reduction of nonlinear wave speeds is not sensible for the classical HLLC formulation, a new centralized reformulation of the HLLC flux is derived. This alternative formulation allows for an analogous reduction of acoustic dissipation as with the modified Roe scheme without introducing additional difficulties. Most of the present shock-stabilizing variants of the HLLC flux restore the shock stability by adding additional dissipation in one way or the other, as motivated by the stability of the stable, but highly dissipative HLL scheme. In contrast, the proposed HLLC-LM flux with *less numerical dissipation* than the classical HLLC flux represents a fundamentally different approach in comparison to the earlier HLLC-HLL combination models. Moreover, in this paper the shock stability of both HLLC and HLLC-LM is studied using high-order methods in space and time, unlike the low-order examples presented in most of the aforementioned publications. We also investigate the grid-aligned shock instability for the HLLC solver in three dimensions and reveal that carbuncles are more likely to occur than in two dimensions.

The paper is organized as follows. In Section 2, the governing equations and the general framework of Godunov-type methods are reviewed together with the classical HLLC flux formulation. A centralized formulation of the HLLC flux is derived in the first part of Section 3, followed by the low Mach number adapted wave speed formulations resulting in the newly proposed HLLC-LM scheme. In Section 4, a comprehensive set of test cases is studied to verify the accuracy and shock stability of the new scheme. Results are also provided with high resolution including a study of three-dimensional effects. Finally in Section 5, calculations of complex flow phenomena that take advantage of the applied high-order schemes, such as a flow around a diamond and multi-component flows with nontrivial shock-interface interactions, are studied to further demonstrate both the stability and the reduced numerical dissipation of the HLLC-LM flux. Conclusions are drawn in Section 6.

2. Governing equations and numerical approach

We consider an inviscid compressible flow that evolves according to the three-dimensional Euler equations

$$\mathbf{U}_t + \mathcal{F}(\mathbf{U})_x + \mathcal{G}(\mathbf{U})_y + \mathcal{H}(\mathbf{U})_z = 0, \tag{1}$$

where $\mathbf{U}$ is the density of the conserved quantities mass ρ, momentum $\rho\mathbf{v} \equiv (\rho u, \rho v, \rho w)$ and total energy $E = \rho e + \frac{1}{2}\rho\mathbf{v}^2$, with e being the internal energy per unit mass. The fluxes $\mathcal{F}$, $\mathcal{G}$ and $\mathcal{H}$ are defined as

$$\mathcal{F} = \begin{pmatrix} \rho u \\ \rho u^2 + p \\ \rho u v \\ \rho u w \\ u(E+p) \end{pmatrix}, \quad \mathcal{G} = \begin{pmatrix} \rho v \\ \rho u v \\ \rho v^2 + p \\ \rho v w \\ v(E+p) \end{pmatrix}, \quad \mathcal{H} = \begin{pmatrix} \rho w \\ \rho u w \\ \rho v w \\ \rho w^2 + p \\ w(E+p) \end{pmatrix}. \tag{2}$$

The set of equations is closed by the ideal-gas equation of state, where the pressure p is given by $p = (\gamma - 1)\rho e$ with a constant ratio of specific heats γ.

2.1. Finite volume approach

Our numerical framework is identical to the one described in [8], where Godunov's approach [1] for finite volumes is applied to solve the given set of equations. The time evolution of the vector of cell-averaged conservative states $\bar{\mathbf{U}}$ is given by

$$\frac{d}{dt}\bar{\mathbf{U}}_i = \frac{1}{\Delta x}(\mathbf{F}_{i-\frac{1}{2},j,k} - \mathbf{F}_{i+\frac{1}{2},j,k} + \mathbf{G}_{i,j-\frac{1}{2},k} - \mathbf{G}_{i,j+\frac{1}{2},k} + \mathbf{H}_{i,j,k-\frac{1}{2}} - \mathbf{H}_{i,j,k+\frac{1}{2}}), \tag{3}$$

where Δx is the cell size of a uniform Cartesian grid and $\mathbf{F}$, $\mathbf{G}$ and $\mathbf{H}$ approximate the cell-face fluxes in x-, y- and z-direction, respectively. These fluxes are determined dimension-by-dimension from a Riemann solver combined with a high-order WENO spatial reconstruction scheme [26]. Additional volume source terms, such as gravitational acceleration, are omitted here for simplicity. The resulting system of ODE (3) is integrated in time using a high-order strong stability-preserving (SSP) Runge-Kutta scheme [27].

2.2. The HLLC Riemann solver

In order to avoid computationally expensive iterative solution of the Riemann problem, approximate Riemann solvers are commonly employed. In this paper, we focus on one specific approximation, the HLLC solver, which is one of the most popular and versatile Riemann solvers. It has been extended to a broad range of applications, also beyond classical computational fluid dynamics [11].

Toro et al. [4] define the HLLC flux as

$$\mathbf{F}^{HLLC} = \begin{cases} \mathbf{F}_L & \text{if } S_L \geq 0, \\ \mathbf{F}_{*L} = \mathbf{F}_L + S_L \cdot (\mathbf{U}_{*L} - \mathbf{U}_L) & \text{if } S_L < 0 \cap S_* \geq 0, \\ \mathbf{F}_{*R} = \mathbf{F}_R + S_R \cdot (\mathbf{U}_{*R} - \mathbf{U}_R) & \text{if } S_R > 0 \cap S_* \leq 0, \\ \mathbf{F}_R & \text{if } S_R \leq 0, \end{cases} \tag{4}$$

where two intermediate states, $\mathbf{U}_{*L}$ and $\mathbf{U}_{*R}$, are separated by the contact wave and are determined from

$$\mathbf{U}_{*K} = \frac{S_K - u_K}{S_K - S_*} \begin{pmatrix} \rho_K \\ \rho_K S_* \\ \rho_K v_K \\ \rho_K w_K \\ E_K + (S_* - u_K)\left(\rho_K S_* + \frac{p_K}{S_K - u_K}\right) \end{pmatrix} \tag{5}$$

with $K = L, R$, and $\mathbf{U}_L$, $\mathbf{U}_R$ being the reconstructed left and right face states, respectively.

Following Einfeldt [9], the maximum left and right nonlinear signal speed estimates are obtained from

$$S_L = \min(u_L - c_L, \hat{u} - \hat{c}), \qquad S_R = \max(u_R + c_R, \hat{u} + \hat{c}), \tag{6}$$

where $\hat{u}$ and $\hat{c}$ are determined from the Roe average

$$\hat{u} = \frac{u_L \cdot \sqrt{\rho_L} + u_R \cdot \sqrt{\rho_R}}{\sqrt{\rho_L} + \sqrt{\rho_R}} \tag{7}$$
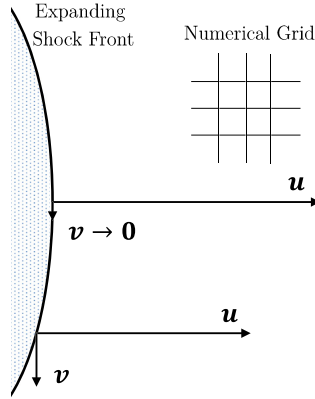
Fig. 1. Schematic illustration of the vanishing velocity component v in transverse direction of the shock front propagation.

and

$$\hat{c}^2 = \frac{c_L^2 \cdot \sqrt{\rho_L} + c_R^2 \cdot \sqrt{\rho_R}}{\sqrt{\rho_L} + \sqrt{\rho_R}} + \frac{1}{2} \frac{\sqrt{\rho_L}\sqrt{\rho_R}}{\left(\sqrt{\rho_L} + \sqrt{\rho_R}\right)^2} (u_R - u_L)^2 . \tag{8}$$

The contact wave speed is estimated according to Batten et al. [12] from

$$S_* = \frac{p_R - p_L + \rho_L u_L (S_L - u_L) - \rho_R u_R (S_R - u_R)}{\rho_L (S_L - u_L) - \rho_R (S_R - u_R)}. \tag{9}$$

High-order approximations for the left and right face states, $\mathbf{U}_L$ and $\mathbf{U}_R$, are obtained upon characteristic decomposition in combination with a high-order WENO scheme as described in detail in [28].

3. A shock-stable HLLC type solver with low Mach number modification

An inaccurate scaling behavior of the acoustic and advection contribution to the numerical dissipation in the low Mach number limit has been found to be the driving mechanism of the numerical grid-aligned shock instability [8]. The connection is motivated by the observation, that shock instabilities only occur when a high Mach number shock wave propagates almost perfectly aligned with the computational grid.

When the shock wave moves in x-direction as shown in Fig. 1, the velocity components of the local transverse direction v, respectively v and w for the three-dimensional case, have a vanishing magnitude. Consequently, the local directional Mach number will also vanish during the computation of the fluxes in transverse directions of the shock wave propagation. Note that a perfect alignment with zero Mach number in transverse directions leads to a one-dimensional situation where no instability occurs. A small deflection is always required to trigger the instability. There is a thorough documentation of the shortcomings of Riemann solvers in the low Mach regime [29–31] which dates back to the findings of Guillard et al. [32,33]. In [32], the authors showed that a wrong scaling behavior of the numerical dissipation leads to pressure fluctuations that may ruin the prediction of low Mach number flows using Godunov's approach. This flaw is now considered as the driving mechanism of the grid-aligned shock instability. In their recent publication, Chen et at. [34] performed a stability analysis to investigate the shock instability mechanism for simplified systems. Their results support the given argumentation as the authors also detect an inaccurate pressure dissipation of the Riemann solver at the vertical transverse face of the shock to be the driving mechanism for the instability. A minor modification that reduces the acoustic dissipation of the Roe Riemann solver in the low Mach number limit proved to be effective in suppressing the instability [8]. The reduction of acoustic dissipation can be achieved by reduction of the nonlinear eigenvalues of the Roe dissipation matrix for small Mach numbers. This procedure stabilizes simulations of supersonic flows. For dealing with global low Mach number flows near the incompressible limit, there are other methods available in literature [29–31].

A straightforward modification of the nonlinear signal speeds of the HLLC solver following [8] turns out to be ineffective in suppressing grid-aligned shock instabilities. The reason for the ineffectiveness can be found when the limit solution of the Roe-M flux and a modified HLLC flux with similarly reduced nonlinear signal speed are compared for vanishing Mach numbers. While the Roe-M approximation [8] reduces in the low Mach number limit to the central flux term

$$\mathbf{F}^{Roe-M} \xrightarrow{Ma \to 0} \frac{1}{2} (\mathbf{F_L} + \mathbf{F_R}) , \tag{10}$$

a modified HLLC approximation with identical reduction of nonlinear signal speeds results in

$$\mathbf{F}^{HLLC-REDUCED} \xrightarrow{Ma\to0} \begin{cases} \mathbf{F}_L & \text{if } S_* \geq 0, \\ \mathbf{F}_R & \text{if } S_* \leq 0. \end{cases} \tag{11}$$

Thus, differently from the limit solution of the Roe-M scheme, a straightforward modification of the HLLC flux leads to a pure classical upwind scheme. Upwinding is not required in the absence of shocks and, moreover, introduces an undesirable amount of numerical dissipation, which counteracts the objective of reducing dissipation. Thus, the goal is to find a formulation of the HLLC flux that continuously approaches the central flux term in the limit of low Mach numbers.

3.1. Central formulation of the HLLC flux

In a first step, the classical HLLC flux will be reformulated motivated by the derivation of the central Roe flux formulation. The intermediate flux F_{*L} can be determined using two alternative approaches

$$\mathbf{F}_{*L} = \mathbf{F}_L + S_L \left(\mathbf{U}_{*L} - \mathbf{U}_L \right) \tag{12}$$

and

$$\mathbf{F}_{*L} = \mathbf{F}_R + S_R \left(\mathbf{U}_{*R} - \mathbf{U}_R \right) + S_* \left(\mathbf{U}_{*L} - \mathbf{U}_{*R} \right). \tag{13}$$

While the traditional derivation of Eq. (12) applies the Rankine-Hugoniot condition only once starting from the left side, alternatively, the Rankine-Hugoniot condition can also be applied twice starting from the right side, Eq. (13). A central formulation of $\mathbf{F}_{*L}$ can be established by averaging both formulations and is given by

$$\mathbf{F}_{*L} = \frac{1}{2} \left(\mathbf{F}_L + \mathbf{F}_R \right) + \frac{1}{2} \left[S_L \left(\mathbf{U}_{*L} - \mathbf{U}_L \right) + S_* \left(\mathbf{U}_{*L} - \mathbf{U}_{*R} \right) + S_R \left(\mathbf{U}_{*R} - \mathbf{U}_R \right) \right]. \tag{14}$$

Analogously, the right intermediate flux can be determined by

$$\mathbf{F}_{*R} = \mathbf{F}_R + S_R \left(\mathbf{U}_{*R} - \mathbf{U}_R \right) \tag{15}$$

and

$$\mathbf{F}_{*R} = \mathbf{F}_L + S_L \left(\mathbf{U}_{*L} - \mathbf{U}_L \right) + S_* \left(\mathbf{U}_{*R} - \mathbf{U}_{*L} \right) \tag{16}$$

resulting in

$$\mathbf{F}_{*R} = \frac{1}{2} \left(\mathbf{F}_L + \mathbf{F}_R \right) + \frac{1}{2} \left[S_L \left(\mathbf{U}_{*L} - \mathbf{U}_L \right) - S_* \left(\mathbf{U}_{*L} - \mathbf{U}_{*R} \right) + S_R \left(\mathbf{U}_{*R} - \mathbf{U}_R \right) \right]. \tag{17}$$

By comparing Eq. (14) and Eq. (17) we note that only the sign of the third term, which is related to the contact wave, differs for both expressions. Finally, considering the requirement that $\mathbf{F}_{*L}$ is applied if $S_* \geq 0$ and $\mathbf{F}_{*R}$ is applied if $S_* \leq 0$, a central formulation of the HLLC flux is obtained by

$$\mathbf{F}^{HLLC} = \begin{cases} \mathbf{F}_L & \text{if } S_L \geq 0, \\ \mathbf{F}_R & \text{if } S_R \leq 0, \\ \mathbf{F}_* & \text{else} \end{cases} \tag{18}$$

with

$$\mathbf{F}_* = \frac{1}{2} \left(\mathbf{F}_L + \mathbf{F}_R \right) \frac{1}{2} \left[S_L \left(\mathbf{U}_{*L} - \mathbf{U}_L \right) + |S_*| \left(\mathbf{U}_{*L} - \mathbf{U}_{*R} \right) + S_R \left(\mathbf{U}_{*R} - \mathbf{U}_R \right) \right]. \tag{19}$$

3.2. On the numerical dissipation of HLL(C)-type solvers

Using the centralized formulation derived in Section 3.1 both the HLL and the HLLC flux in the subsonic regime can be written as

$$\mathbf{F}_{HLL} = \frac{1}{2} \left(\mathbf{F}_L + \mathbf{F}_R \right) - \frac{1}{2} \left[|S_L| \left(\mathbf{U}_* - \mathbf{U}_L \right) + |S_R| \left(\mathbf{U}_R - \mathbf{U}_* \right) \right]$$

$$\mathbf{F}_{HLLC} = \frac{1}{2} \left(\mathbf{F}_L + \mathbf{F}_R \right) - \frac{1}{2} \left[|S_L| \left(\mathbf{U}_{*L} - \mathbf{U}_L \right) + |S_*| \left(\mathbf{U}_{*R} - \mathbf{U}_{*L} \right) + |S_R| \left(\mathbf{U}_R - \mathbf{U}_{*R} \right) \right]. \tag{20}$$

A connection to the Lax-Friedrichs flux can be established, when $|S_L| = |S_*| = |S_R| = |\lambda|$ is introduced into $\mathbf{F}_{HLL}$ or $\mathbf{F}_{HLLC}$ resulting in

$$\mathbf{F}_{HLL(C)}^{\lambda} = \frac{1}{2} \left(\mathbf{F}_L + \mathbf{F}_R \right) - \frac{1}{2} |\lambda| \left(\mathbf{U}_R - \mathbf{U}_L \right). \tag{21}$$
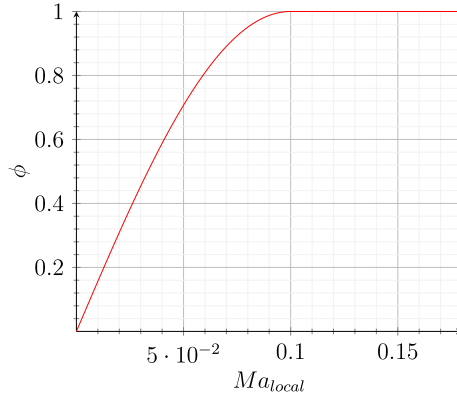
Fig. 2. Dependence of the activation function ϕ on the local Mach number Ma_{local} with $Ma_{limit} = 0.1$.

Now, the HLL(C) flux can be seen as a Lax-Friedrichs flux where the dissipation has been split into two (HLL), or three (HLLC) differently weighted contributions representing the general wave system of the underlying Riemann problem.

In the original formulation of the HLLC approximation (4), advection and acoustic contributions to the numerical dissipation are difficult to separate. However, the proposed central formulation of the HLLC solver allows for a separation of both contributions in analogy with the Roe flux, which is given by

$$\mathbf{F}_{Roe} = \frac{1}{2} \left(\mathbf{F}_L + \mathbf{F}_R \right) - \frac{1}{2} \mathbf{R} |\mathbf{\Lambda}| \mathbf{R}^{-1} \left(\mathbf{U}_R - \mathbf{U}_L \right). \tag{22}$$

The first part both in Eq. (19) and Eq. (22) is the central flux term, and the second term is the dissipation flux term, which is characteristic for each solver. The advection dissipation of the Roe flux is proportional to the eigenvalue $|u|$, and the acoustic dissipation of the Roe flux is proportional to the eigenvalues $|u \pm c|$. Analogously, the acoustic dissipation of the HLLC flux is related to the first and third term of the dissipation flux term as both terms are proportional to the acoustic signal speed S_L, respectively S_R. The advection dissipation is related to the center term, which is proportional to the contact signal speed S_*. Note that the situation for the HLLC flux is more complex than for the Roe flux since S_L and S_R also contribute to S_*, $\mathbf{U}_{*L}$ and $\mathbf{U}_{*R}$. However, the results of this paper indicate that the main contributions of advection and acoustic dissipation can be distinguished as discussed.

3.3. HLLC-LM flux with low Mach number correction

The main goal of the proposed modification is to balance the vanishing advective and dominant acoustic dissipation in the low Mach number limit by a reduction of overall dissipation. The central formulation of the HLLC flux given by Eq. (18) and Eq. (19) enables a straightforward application of the Mach number dependent reduction of nonlinear signal speeds according to

$$S_L^{HLLC-LM} = \phi \cdot S_L, \qquad S_R^{HLLC-LM} = \phi \cdot S_R \tag{23}$$

with

$$\phi = \sin \left(\min \left(1, \frac{Ma_{local}}{Ma_{limit}} \right) \cdot \frac{\pi}{2} \right) \tag{24}$$

and

$$Ma_{local} = \max \left(\left| \frac{u_L}{c_L} \right|, \left| \frac{u_R}{c_R} \right| \right). \tag{25}$$

u denotes the velocity component dependent on the direction of the cell-face Riemann problem. $S_L^{HLLC-LM}$ and $S_R^{HLLC-LM}$ are only applied for the final flux evaluation in Eq. (19). All previous procedures, especially the calculation of S_*, $\mathbf{U}_{*L}$ and $\mathbf{U}_{*R}$, are performed using the original values for S_L and S_R.

The application of the sine function in Eq. (24) causes a smooth decay of the acoustic dissipation as depicted in Fig. 2. The reference parameter Ma_{limit} is set to 0.1 for all calculations presented in this paper. This selection ensures that the modification will only be active if the local flow speed component is less than ten percent of the local sound speed. Otherwise, the classical HLLC formulation is fully recovered. The new scheme, denoted as HLLC-LM in the following, fully preserves the favorable low dissipation of HLLC at the contact line as the acoustic dissipation of HLLC-LM is reduced proportionally to the level of local velocities instead of the speed of sound for low Mach numbers while the advection dissipation remains unchanged.
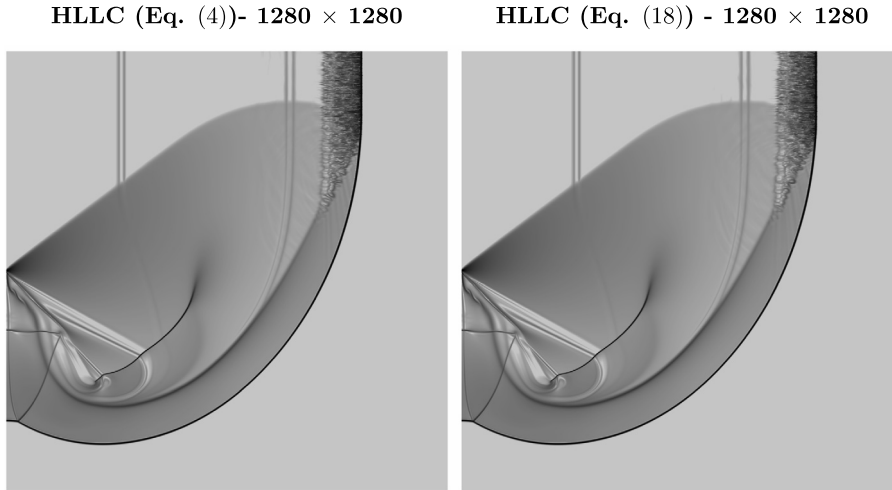
HLLC (Eq. (4))- 1280 × 1280   HLLC (Eq. (18)) - 1280 × 1280

Fig. 3. Comparison of the classical HLLC formulation with the central HLLC formulation for the corner diffraction of a Mach 5.09 shock wave: logarithmic gradients of density from 1 to 1,000 at $t = 0.157$.

4. Central aspects of the grid-aligned shock instability with HLLC-type solvers demonstrated for classical test cases

The calculations in this section serve to study the evolution of the numerical shock instability when HLLC-type solvers are applied in combination with high-order schemes. Moreover, the stability of the HLLC-LM scheme with respect to the grid-aligned shock problem is demonstrated for a comprehensive set of cases with strong moving shocks that are prone to exhibiting this instability. If not mentioned otherwise, all calculations were performed using the classical fifth-order WENO scheme [26] for spatial discretization combined with a third-order strong-stability-preserving Runge-Kutta time integration [27] and the approximate Riemann solvers as described in the previous sections. The effective range of the shock-transverse Mach number modification in the HLLC-LM solver is always limited to local Mach numbers lower than 0.1. The fluid is modeled as ideal gas with $\gamma = 1.4$. The CFL number is set 0.6 for single-phase cases and 0.4 for cases with interfaces employing the level-set approach. The combination of a multiresolution procedure [35] and an adaptive local time stepping [36] enables efficient computation with high effective resolutions. In the following, the given resolution information defines the finest level. Shocks are discretized with the highest resolution in all presented cases due to the applied refinement criteria, whereas material interfaces are by definition on the highest level.

4.1. Corner flow problem I: verification of centralized HLLC formulation

As a first step, the proposed centralized HLLC formulation given in Eq. (18) and Eq. (19) is verified against the classical HLLC procedure for the diffraction of a shock wave around a sharp corner. This is a well-established test case, where the instability of the HLLC flux becomes apparent. This case was already selected by Quirk [6] to demonstrate the failure of low-dissipation Riemann approximations. Additionally, the problem yields complex flow patterns. Thus, it is well suited to compare results of different solvers and to verify our reformulations.

We use a domain of size $[0, 1] \times [0, 1]$, that is uniformly initialized with $(\rho, u, v, p) = (1, 0, 0, 1/1.4)$ and discretized by 1280×1280 cells. Reflecting-wall boundary conditions are set everywhere, except for the upper left boundary at $x = 0$ from $y = 0.5$ to $y = 1$. Here, the post-shock condition of a Mach 5.09 shock wave is prescribed. The final time is set to $0.8/Ma$. Even though the first-order HLLC approximation is known to be positivity preserving, this property is not guaranteed for high-order extensions [37]. We encountered instabilities in the vicinity of the corner point of the backward facing step at the inflow for all tested variants of the HLLC flux when combined with a fifth-order WENO scheme. Therefore, simulations were performed using a third-order WENO scheme [26].

Fig. 3 and Fig. 4 show schlieren images of the density gradients at the final time of the simulation. The results shown in the left frame of Fig. 3 are obtained applying the original HLLC formulation given in Eq. (4), whereas results shown in the right frame of Fig. 3 are obtained applying the centralized HLLC formulation given in Eq. (18) and Eq. (19). As expected, there are no distinguishable differences for both formulations. Moreover, all other test cases presented in this paper have been investigated without encountering any differences exceeding the floating-point roundoff error. We therefore conclude that Eq. (18) with Eq. (19) is a valid alternative representation of the HLLC flux.

4.2. Corner flow problem II: stability of HLLC-LM formulation

As a second step, the stability of the HLLC-LM scheme is demonstrated. The aforementioned corner flow simulations show severe disturbances in the backflow of the leading shock front similar to results obtained with the Roe Riemann
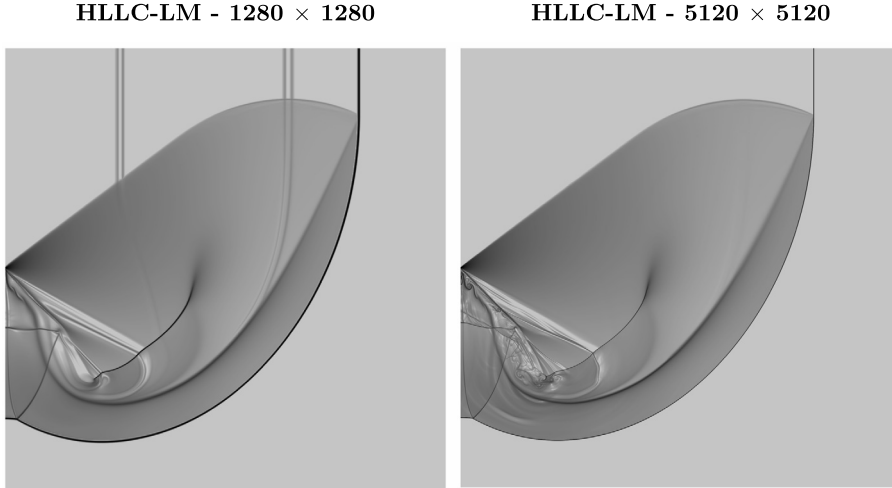
HLLC-LM - 1280 × 1280   **HLLC-LM - 5120 × 5120**

Fig. 4. Corner diffraction of a Mach 5.09 shock wave: logarithmic gradients of density from 1 to 1, 000 at $t = 0.157$.

solver [6]. The left frame of Fig. 4 shows that the HLLC-LM is able to capture all details of the flow while preventing any disturbances of the shock wave. Additionally, a high-resolved simulation is performed using 16 times smaller cells. Typically, the instability is enhanced by higher resolutions, however, the results presented in the right frame of Fig. 4 are still free of any instability.

4.3. Rayleigh Taylor instability: numerical dissipation at contact lines

The inherent numerical dissipation of the original HLLC flux and HLLC-LM flux is compared by investigating a classical Rayleigh-Taylor instability. Two initial gas layers with different densities are exposed to gravity with unity magnitude, where the resulting acceleration is directed towards the lighter fluid. A small disturbance of the contact line triggers the instability. The computational domain is given by $[0, 0.25] \times [0, 1]$ and the interface initially is placed at $y = 0.5$. Initial states are given by $(\rho, u, v, p)_{y \leq 0.5} = (2, 0, -0.025c \cdot cos(8\pi x), 2y + 1)$ and $(\rho, u, v, p)_{y > 0.5} = (1, 0, -0.025c \cdot cos(8\pi x), y + 1.5)$, where the speed of sound is $c = \sqrt{\frac{\gamma p}{\rho}}$ with $\gamma = \frac{5}{3}$. Top and bottom boundary states are fixed to $(1, 0, 0, 2.5)$ and $(2, 0, 0, 1)$, respectively. Symmetry boundary conditions are imposed at the left and right boundary.

The final density evolution for both solvers is shown in Fig. 5 for a resolution of 128×512. Results indicate a significant reduction of dissipation at the contact line when the HLLC-LM flux is applied instead of the original HLLC flux.

4.4. Quirk's odd-even decoupling test: quantitative evaluation of the shock instability

The results of the Section 4.2 indicate the effectiveness of the proposed method qualitatively, however, a detailed quantitative study is difficult to perform for the corner flow problem. For this purpose, the simple plane shock propagation along a rectangular duct with a defined disturbance level is studied. This test case was also proposed by Quirk [6] due to its simple setup. Nevertheless, it provides an effective and reliable way to trigger the odd-even decoupling near strong shocks, which is related to the grid-aligned shock instability. Moreover, it allows for a simple quantitative study of the rise of the instability.

The domain is set to $[0, 2400] \times [0, 20]$, and discretized with 2400×20 cells. Inflow and outflow conditions are applied at the left and at the right boundary, respectively. Reflecting wall conditions, which are equivalent to symmetry boundary conditions for inviscid flows, are enforced both at the top and at the bottom boundary of the domain. Pre-shock density and pressure are set to unity, and all velocity components are set to zero. Artificial numerical noise is introduced to all primitive variables in the initial state to trigger the instability [38,8]. We have performed simulations with the original Mach 6 setup and with a Mach 20 setup with initial conditions given by

$$(\rho, u, v, p) = \begin{cases} (1, 0, 0, 1) & \text{if } x > 5, \\ \left(\frac{216}{41}, 35\frac{\sqrt{35}}{36}, 0, \frac{251}{6}\right) & \text{else (for } Ma = 6 \text{ case)}, \\ \left(\frac{160}{27}, \frac{133}{8}\sqrt{1.4}, 0, 466.5\right) & \text{else (for } Ma = 20 \text{ case)}, \end{cases} \tag{26}$$

where the shock front is initially placed at $x = 5$. Both simulations are performed up to a late point in time till the shock front approaches the end of the domain. The final time is set to 330 for the low Mach number simulation and to 100 for the high Mach number simulation, respectively.
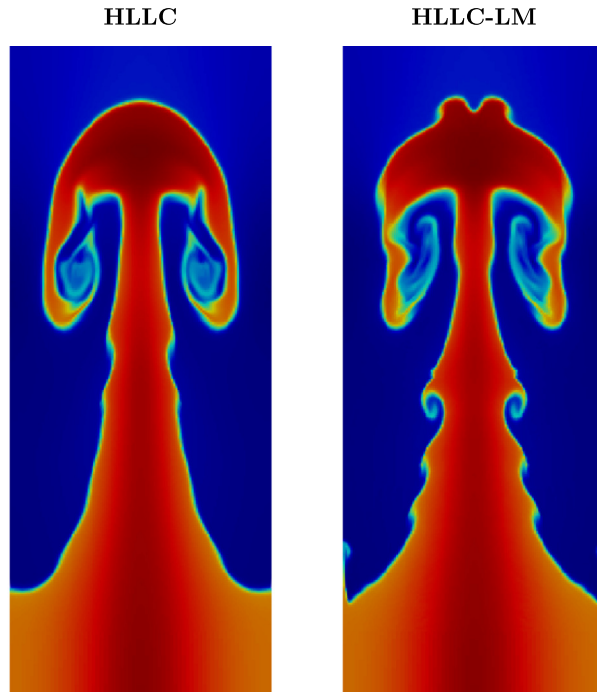
HLLC   HLLC-LM

Fig. 5. Rayleigh-Taylor instability $t = 1.95$: density contours from 0.85 (blue) to 2.25 (red). (For interpretation of the colors in the figure(s), the reader is referred to the web version of this article.)
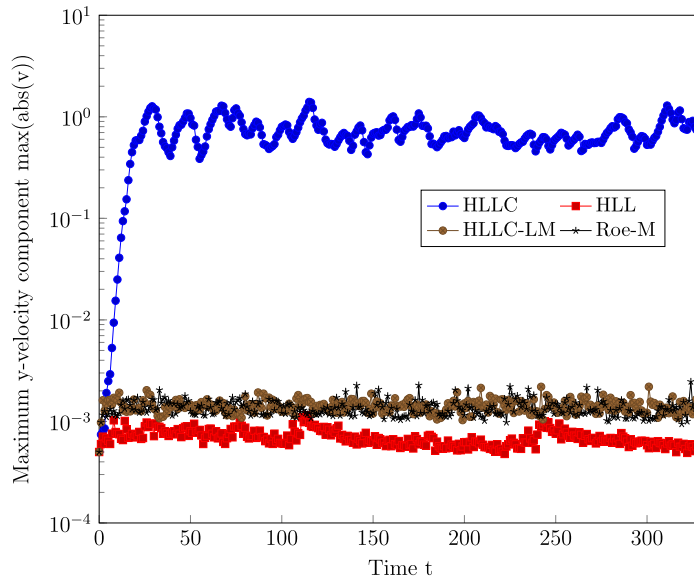

Fig. 6. Instability progress in Quirk's test case for Mach 6.

The maximum magnitude of the y-velocity component v in the domain provides a reasonable measure of the deviation from the one-dimensional solution, and therefore, it is well suited to monitor the growth rate of the disturbance quantitatively over time. Fig. 6 and Fig. 8 show the evolution of the velocity deviation for the Mach 6 and the Mach 20 case for different flux approximations when all initial primitive variables are superposed by uniform random perturbations ranging from $-0.5 \cdot 10^{-3}$ to $0.5 \cdot 10^{-3}$. In addition, the final density distributions are presented in Fig. 7 and Fig. 9. Besides the results for the discussed HLLC and HLLC-LM fluxes, the results for the more dissipative HLL flux [3] and the shock-stable Roe-M flux [8] are provided for comparison.

Simulations with the classical HLLC solver show an exponential instability where instabilities saturate at $\mathcal{O}(1)$ at around $t = 20$ for the low Mach number case and at around $t = 5$ for the high Mach number case. Unlike the Roe approximation,
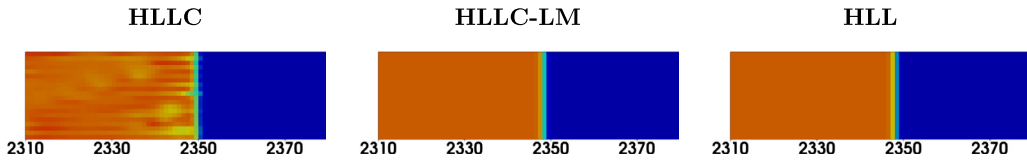
Fig. 7. Quirk's test case for Mach 6: color map of density from blue = 1.0 to red = 6.8 at $t = 330$.
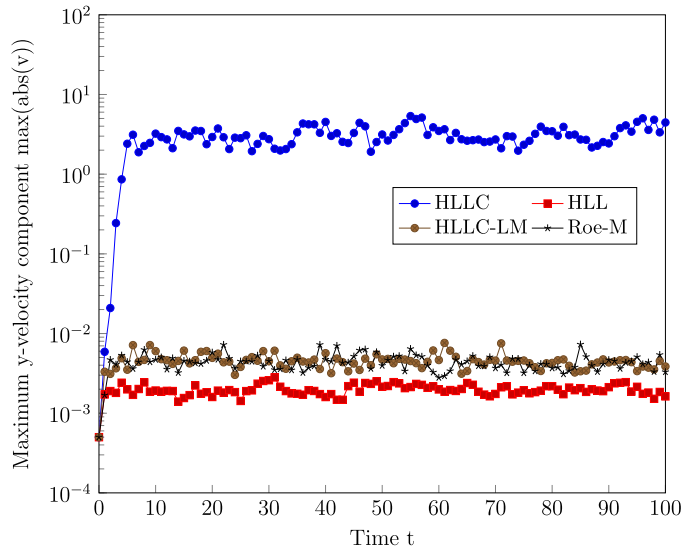

Fig. 8. Instability progress in Quirk's test case for Mach 20.
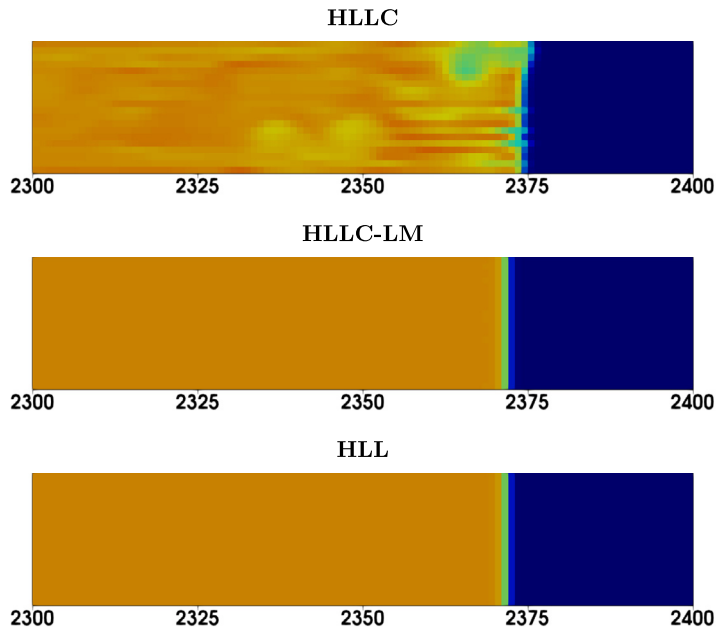

Fig. 9. Quirk's test case for Mach 20: color map of density from blue = 1.0 to red = 8.0 at $t = 100$.

the HLLC flux forms no distinct carbuncles, and density disturbances remain bounded. However, the instability disturbs the shock front significantly as shown in the left frame, respectively top frame, of Fig. 7 and Fig. 9. Moreover, when the final position of the shock front is compared to the analytically predicted position, an incorrect wave speed is obtained. This effect is even more dominant for the high Mach number case. With the modified HLLC-LM scheme, the stable and analytically predicted result is obtained as depicted in the middle frames of Fig. 7 and Fig. 9. The magnitude of disturbances
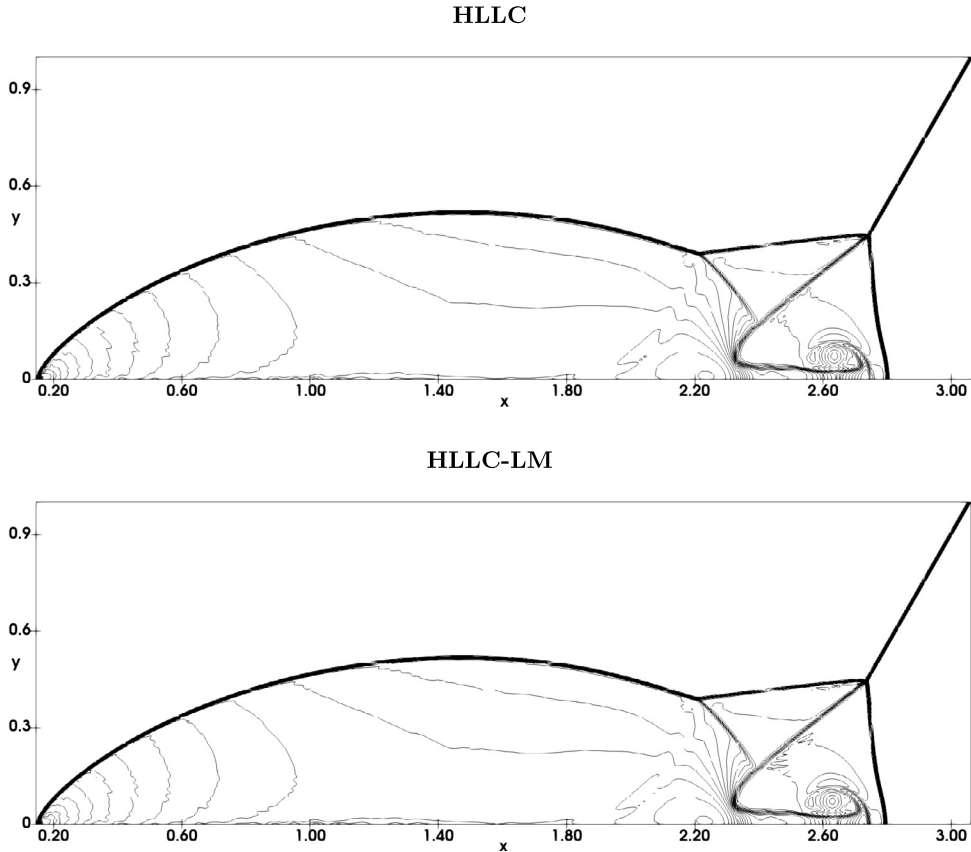
HLLC

HLLC-LM

Fig. 10. Double Mach reflection of a Mach 10 shock wave: 40 density contours from 1.88783 to 20.9144 at $t = 0.2$.

is similar to the one obtained with the Roe-M formulation [8] and slightly higher than the one obtained with the HLL flux for both cases. The lower disturbances of the HLL flux can be explained by a significantly higher level of inherent dissipation of the scheme. However, no major differences can be observed in the qualitative density results for HLL and HLLC-LM, e.g. middle and bottom frame of Fig. 9.

4.5. Double Mach reflection problem: effect of resolution

Several numerical schemes encounter difficulties when simulating a double Mach reflection as proposed by Woodward and Colella [39]. The leading Mach stem may be kinked in consequence of the numerical shock instability [6,7]. The test case represents a Mach 10 shock wave hitting a solid ramp with an angle of 30 degrees. The initial shock wave is set up with

$$(\rho, u, v, p) = \begin{cases} (1.4, 0, 0, 1) & \text{if } y < \sqrt{3}\,(x - 1/6)\,, \\ \left(8, 33\frac{\sqrt{3}}{8}, -4.125, 116.5\right) & \text{else.} \end{cases} \tag{27}$$

A Neumann boundary condition with zero gradients for all variables is applied at the left, right and upper boundary. Along the bottom boundary, at $y = 0$, the region from $x = 0$ to $x = 1/6$ is always assigned post-shock conditions, whereas reflecting-wall conditions are imposed from $x = 1/6$ to $x = 4$. The domain size of $[0, 4] \times [0, 6.67]$ is chosen large enough to avoid any disturbances entering the domain at the upper boundary. The domain is discretized with 960×1600 cells and the final time is set to $t = 0.2$. Besides the large vertical domain size, this setup is commonly chosen in literature [40].

The final density contours for both HLLC and HLLC-LM are shown in Fig. 10. Both schemes deliver almost identical results with no visible deflection at the leading Mach stem. However, if the resolution is increased to 1920×3200 cells and the final time is set to $t = 0.28$ the results for both schemes differ significantly as shown in Fig. 11. A kinked Mach stem, together with a severe disturbance of the wall jet can be observed for the original HLLC scheme, whereas the HLLC-LM scheme is free of any instability.
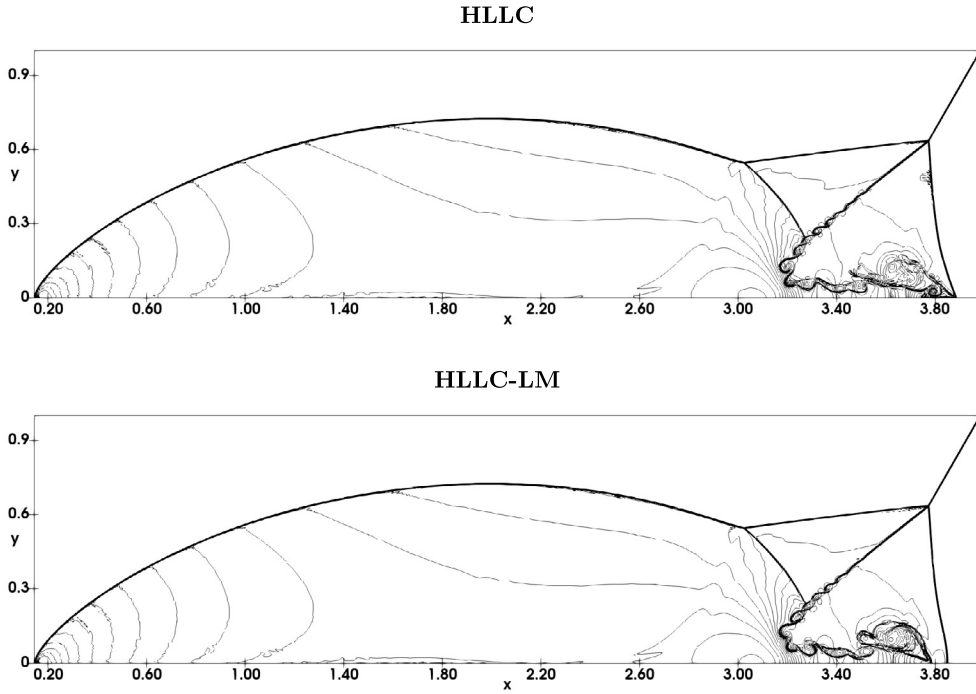
HLLC

HLLC-LM

Fig. 11. Double Mach reflection of a Mach 10 shock wave: 40 density contours from 1.88783 to 20.9144 at $t = 0.28$.

4.6. Supersonic flow around cylinder: steady shock position

The next case predicts the bow shock resulting from a supersonic flow around a stationary cylinder. This case was first described by Peery and Imlay [5] to suffer from the carbuncle phenomenon. Unlike the other cases in this paper, the relevant shock wave is not moving, which renders the case particularly challenging for high-order shock-capturing schemes with explicit time integration. Following the argumentation in [8], we do not change the Cartesian grid nor the time integration, which likely results in a small resolved level of fluctuations around the steady shock due to the high order of the applied scheme. We include this case for the sake of completeness even though the application of high-order schemes here is not expected to reveal additional information for such configurations compared to low-order schemes.

The circular reflecting-wall condition representing the cylinder is approximated using a level-set approach [41]. At the left and the remaining right boundary inflow and outflow conditions are applied, respectively. Top and bottom boundary conditions are set to Neumann boundary conditions with zero gradient for all variables. Two different Mach numbers, $Ma = 3$ and $Ma = 20$, are studied with initial states $(\rho, u, v, p) = \left(1, \sqrt{1.4} \cdot Ma, 0, 1\right)$. The domain size is set to $[0, 0.3] \times [0, 0.8]$ for the lower Mach number, and $[0, 0.3] \times [0, 0.6]$ for the higher Mach number. Final times are chosen large enough to reach a fully developed bow shock. The cylinder with a diameter $D = 0.2$ is placed at the center of the right boundary and resolved by 160 cells per diameter.

Besides the HLLC and the HLLC-LM schemes, the more dissipative HLL scheme is also applied. Fig. 12 and Fig. 13 show the resulting pressure distributions and Mach contour lines that are chosen identical to [7] for both Mach number flows. All three schemes show comparable results for both Mach numbers. Note that also the HLL scheme reveals some disturbances in the backflow of the steady shock. These disturbances of the HLL scheme in combination with high-order methods have been reported in literature [42]. None of the schemes suffers from the carbuncle phenomenon with the described Cartesian setup. Moreover, the HLLC-LM scheme has been tested for a significantly increased resolution of 640 cells per diameter, where it still delivers stable results as shown in the right frames of Fig. 12 and Fig. 13.

4.7. The Sedov blast wave: comparison of shock instability in two and three dimensions

The next case of this section is the classical Sedov blast wave [43,37,7]. Due to its symmetry, the Sedov blast wave simulation is suitable to demonstrate the effect of the grid alignment on the numerical shock instability [8]. The test case consists of a high pressure area covering only few cells that is initiated at the center of the domain. The rest of the domain is set to a near vacuum state. The whole domain is initially at rest. The initial states are given by

$$(\rho, u, v, p) = \begin{cases} \left(1, 0, 0, 3.5 \cdot 10^5\right), & \text{if } \sqrt{x^2 + y^2} < 0.005, \\ \left(1, 0, 0, 10^{-10}\right), & \text{otherwise.} \end{cases} \tag{28}$$
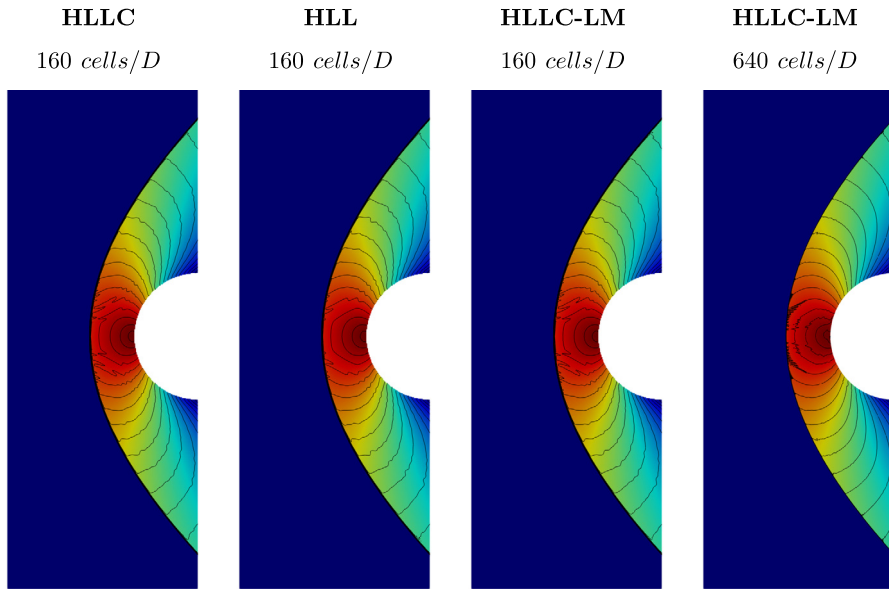
Fig. 12. Supersonic flow around cylinder $Ma = 3$ at $t = 1.5$: color pressure map (blue $= 1.0$ to red $= 12.1$) is overlaid by 25 Mach contours (0.1 to 2.5).
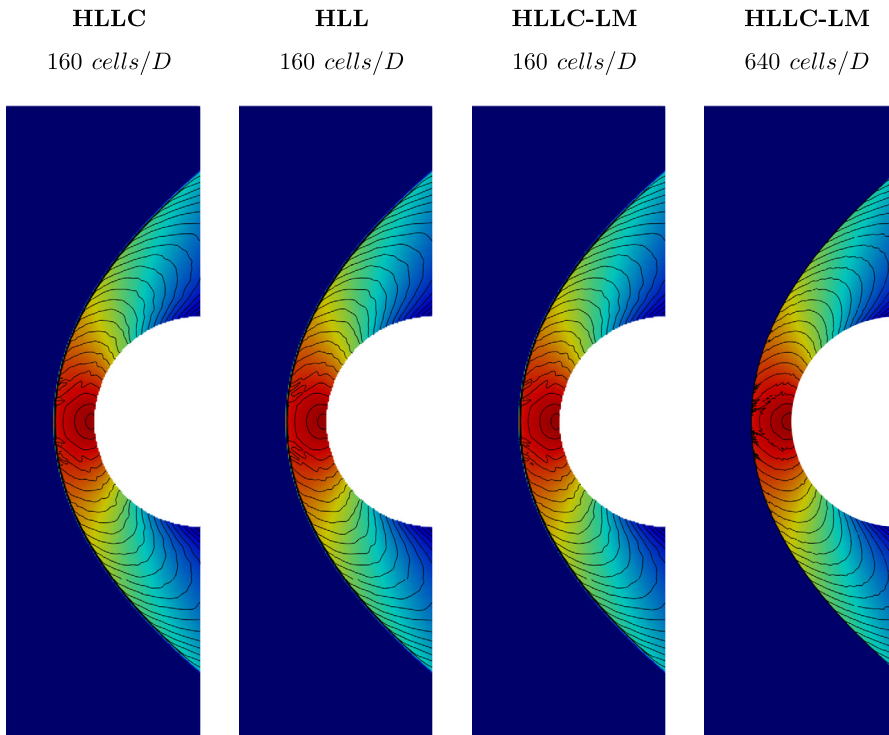

Fig. 13. Supersonic flow around cylinder $Ma = 20$ at $t = 0.5$: color pressure map (blue $= 1.0$ to red $= 550$) is overlaid by 25 Mach contours (0.1 to 2.5).

Reflecting-wall conditions are applied at all boundaries. The domain size is set to $[-1.2, 1.2] \times [-1.2, 1.2]$, and it is resolved by 960×960 cells. The final time is set to 0.1.

The schlieren image for logarithmic density gradients is given in Fig. 14 when using the HLLC flux and the HLLC-LM flux. At locations where the shock front propagates aligned with the computational grid, disturbances behind the shock wave can be observed. The magnitude of disturbances is smaller than for the Roe flux [8] and no carbuncles occur. The results obtained with the HLLC-LM flux are free of any disturbance.

Finally, we extend the problem to three dimensions in a straightforward way. The domain size is set to $[-2, 2] \times [-2, 2] \times [-2, 2]$ and is resolved by a resolution of $640 \times 640 \times 640$ cells. In order to save computational cost, only one-eighth of the
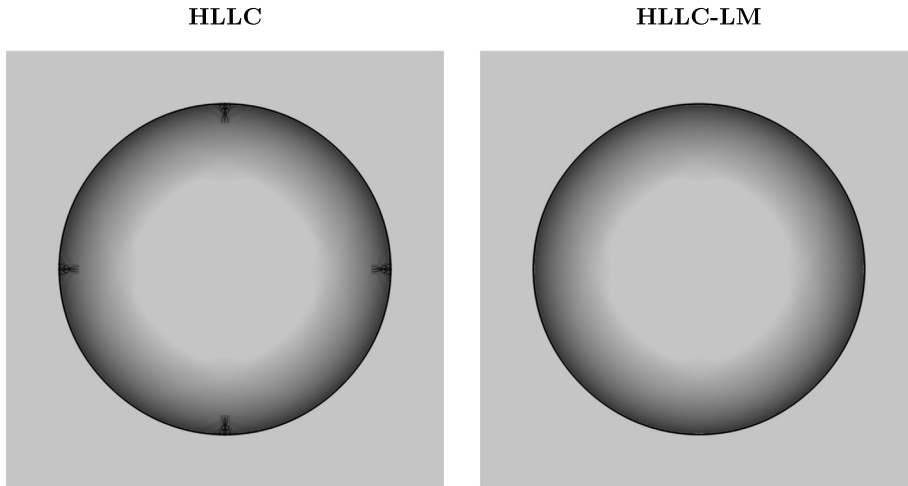
HLLC   HLLC-LM

Fig. 14. Two-dimensional Sedov blast wave: logarithmic gradients of density from 1 to 500 at $t = 0.1$.

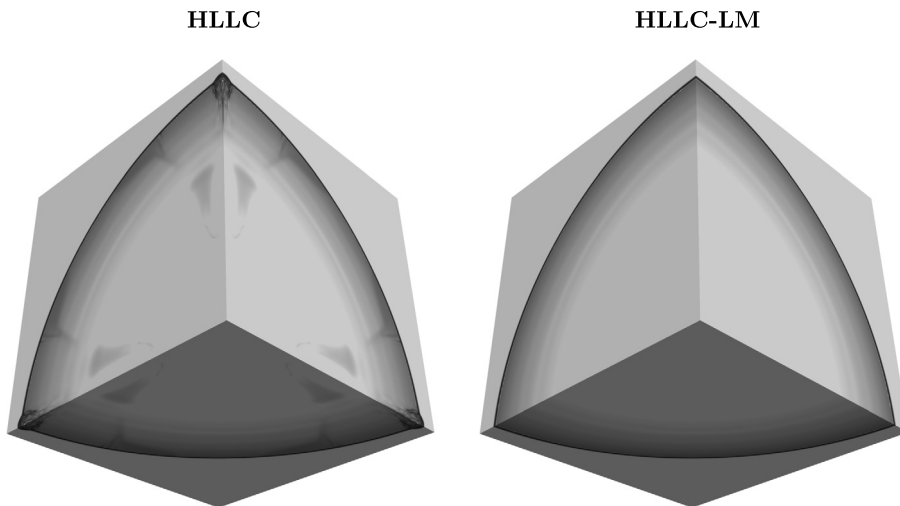HLLC   HLLC-LM

Fig. 15. Three-dimensional Sedov blast wave: logarithmic gradients of density from 1 to 500 at $t = 0.1$.

given domain is simulated and appropriate symmetry boundary conditions are applied. The setup is chosen according to Tasker et al. [43], where initial states are

$$(\rho, u, v, w, p) = \begin{cases} \left(1, 0, 0, 0, 23.757239 \cdot 10^6\right), & \text{if } \sqrt{x^2 + y^2 + z^2} < 0.0875, \\ \left(1, 0, 0, 0, 1 \cdot 10^{-10}\right), & \text{otherwise} \end{cases} \tag{29}$$

with $\gamma = \frac{5}{3}$. The final time again is set to 0.1.

Results for the three-dimensional Sedov blast wave are shown in Fig. 15 for both HLLC and HLLC-LM. Differently from the two dimensional case, the three-dimensional simulation reveals an increased level of disturbances and the occurrence of significant carbuncles for the HLLC flux. This indicates that the instability is enhanced for three-dimensional simulations. Following the argumentation of Section 3, this behavior can be explained as follows. A three-dimensional shock wave that propagates along one coordinate axis suffers from an excessive acoustic dissipation that is now introduced from two sides as the fluxes in both other directions have a vanishing Mach number. As expected, the reduction of acoustic dissipation in the HLLC-LM scheme also helps to prevent the grid-aligned shock instability in three-dimensional simulations.

4.8. Subsonic flow around cylinder: low Mach number flow

In addition to the shock-dominated flow problems presented before, the performance of the proposed HLLC-LM scheme also is tested in the global low Mach number regime using the well-known test case of a subsonic flow around a cylinder.
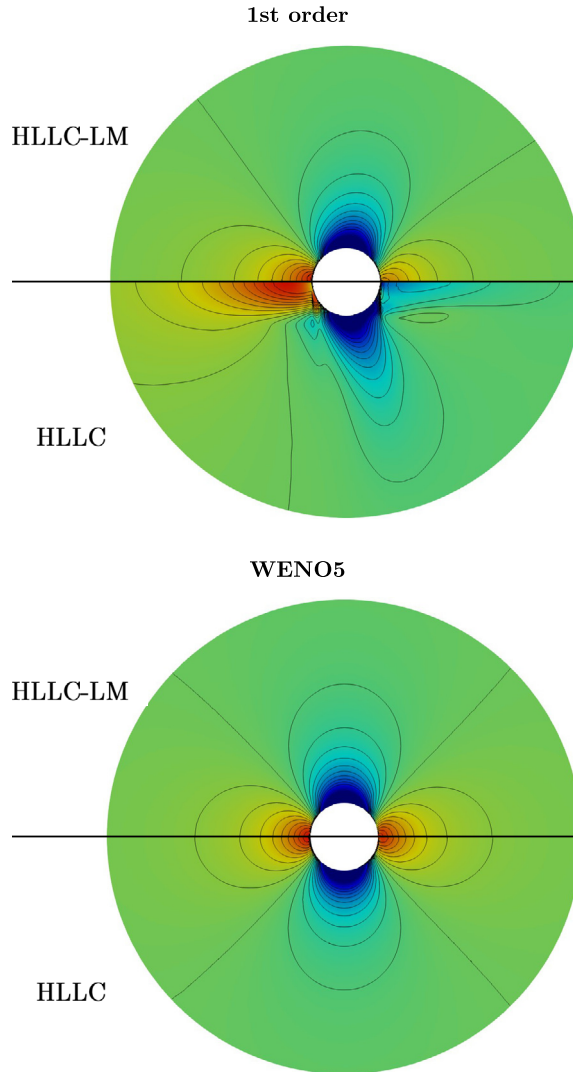
Fig. 16. Flow around a cylinder at $Ma = 0.01$ using first order (top) and WENO5 (bottom): color density map (blue $= 0.99993$ to red $= 1.00007$) is overlaid by 21 contour lines for normalized pressure fluctuations from $-7 \cdot 10^{-5}$ to $7 \cdot 10^{-5}$.

This flow configuration is troublesome for Godunov schemes in combination with Riemann solvers as comprehensively discussed in literature, e.g. [29]. Different modifications to Riemann solvers and preconditioning techniques have been proposed to increase the simulation accuracy of low Mach number flows [32,30,31].

The domain of size $[0, 80D] \times [0, 80D]$ is set large enough to avoid any interaction of reflected waves, which is crucial for the high-order simulation. The cylinder is placed in the center of the domain with a diameter $D = 1$. Initial density and pressure are set to unity in the entire domain. The initial velocity of $u = 0.01 \cdot \sqrt{1.4}$ results in a free-stream Mach number of 0.01. At all boundaries we apply Neumann boundary conditions with zero gradient for all variables. The effective resolution is set to 128 cells per diameter. The final time $t = 30$ is large enough to approach a steady state before disturbances due to reflections at the domain boundaries affect the region of interest around the cylinder. Note that the application of high-order schemes in combination with explicit time integration for the fully compressible evolution equations renders low Mach number simulations particularly expensive.

Fig. 16 shows the density distribution in the relevant region around the cylinder and 21 isocontours for pressure fluctuations $\delta p = p - p_0$ between $\pm \gamma Ma^2/2 = \pm 7 \cdot 10^{-5}$ similarly to [29] for HLLC and HLLC-LM using both a first-order and a WENO5-JS spatial discretization.

The fully symmetric flow field obtained with WENO5 shows excellent agreement with the expected result. In either case, the HLLC-LM solver shows similar or better performance than the original HLLC. Nevertheless, it should be pointed out that the HLLC-LM solver is primarily designed for applications in the high Mach number regime that suffer from shock instabilities. Due to the decreasing numerical dissipation in the low Mach number limit we expect the occurrence of pressure-velocity decoupling when the Mach number is further reduced.
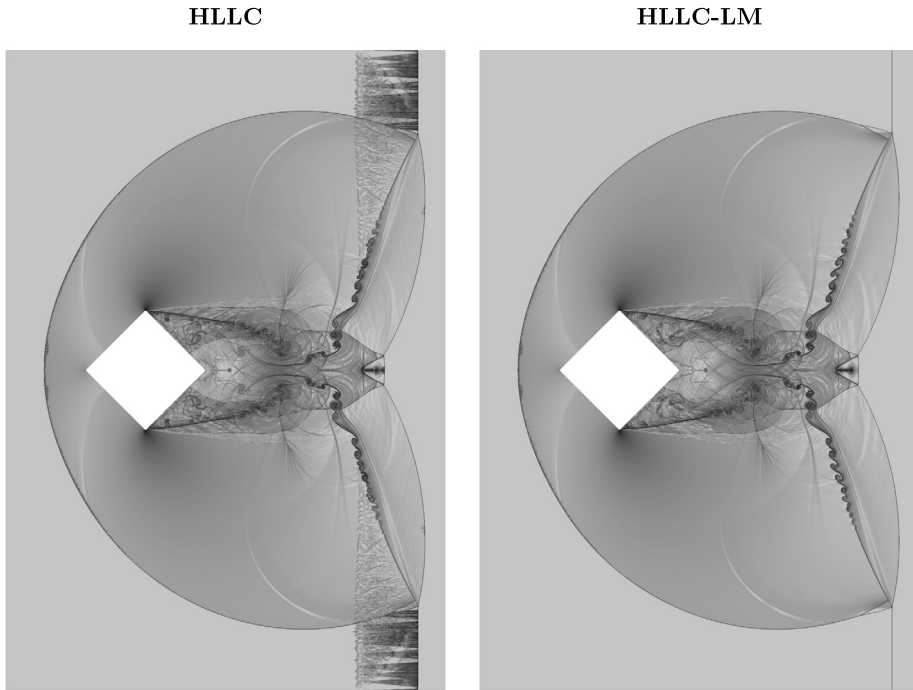
<table>
<tr><td align="center">HLLC</td><td align="center">HLLC-LM</td></tr>
</table>

Fig. 17. Supersonic flow around a diamond-shaped obstacle with $Ma = 2.85$: logarithmic gradients of density from 1 to 1000 at $t = 0.5$.

5. Application to complex flow situations

The main motivation for the application of high-order low-dissipation schemes is an accurate prediction of highly complex flow situations. Therefore, we studied three additional types of test cases that involve interaction of shock waves with nontrivial structures and recent examples of multi-component flow simulations using the level-set approach [41].

5.1. Supersonic flow around diamond-shaped obstacle

The first example of a highly complex flow evolution is the supersonic flow around a diamond-shaped obstacle. The Mach number of 2.85 is chosen to be high enough to form a double Mach reflection during and after the shock wave propagates over the diamond [44]. The sharp geometry changes result in extremely complex flow patterns in the wake of the diamond. In addition to the double Mach reflection, this case also involves a bow shock in front of the obstacle and the classical odd-even decoupling situation near the leading shock wave. This makes the case particularly interesting to study in the context of this paper.

The shock wave is initialized with

$$(\rho, u, v, p) = \begin{cases} (3.714, 2.464, 0, 9.310) & \text{if } x < 0.375 \\ (1, 0, 0, 1) & \text{else,} \end{cases} \tag{30}$$

and the center of the diamond is placed at $x = 0.7$ and $y = 1.6$ with a distance $D = 0.6$ from corner to corner. The domain size is set to $[0, 2.2] \times [0, 3.2]$ and it is discretized with 7040×10240 cells. The final time is set to 0.5. Neumann boundary conditions with zero gradients for all variables are applied at the lower and upper boundary. Inflow and outflow conditions are imposed at the left and right boundary. The reflecting-wall condition representing the diamond is again approximated using a level-set approach [41].

Fig. 17 shows the final schlieren images of density gradients using both HLLC and HLLC-LM. An obvious disturbance behind the leading shock wave develops when the classical HLLC approximation is applied. This is caused by an odd-even decoupling effect, similarly to the corner flow presented in Section 4. Again, the HLLC-LM flux fully removes the disturbance. Note, that the complex flow evolution is not affected by the low Mach number correction. Further details can be observed within the double Mach reflection zone as shown in the zoomed region given in Fig. 18. The proposed HLLC-LM scheme results in a stable and disturbance-free flow field behind the leading Mach stem. Moreover, the decreased numerical dissipation of the HLLC-LM flux becomes apparent when the resolution of the wave patterns is compared.
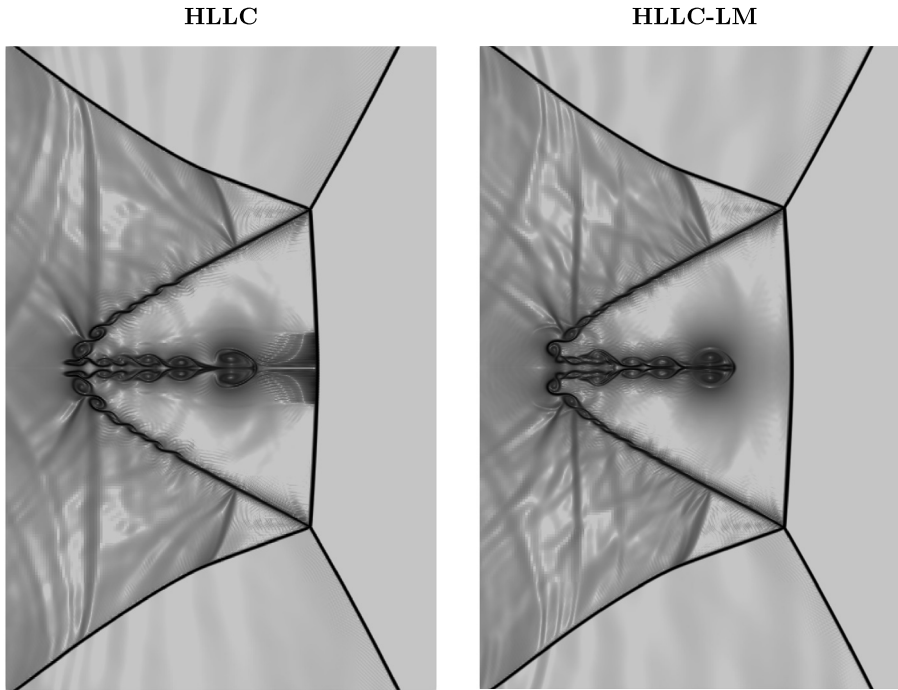
HLLC   HLLC-LM

Fig. 18. Zoom on double Mach reflection in supersonic flow around a diamond-shaped obstacle with $Ma = 2.85$: logarithmic gradients of density from 1 to 1000 at $t = 0.5$.

5.2. Shock interface interaction: helium bubble in air

Another important application of high-order methods is the prediction of multi-component flows. In [8], it was shown that the grid-aligned shock instability limits the numerical investigation of shock-interface interaction problems. The same case of the interaction of a Mach 6 shock wave in air ($\gamma = 1.4$) with a helium bubble ($\gamma = 1.66$) is now studied with HLLC-type solvers.

Initial states are given by

$$(\rho, u, v, p) = \begin{cases} \left(\frac{216}{41}, 35\frac{\sqrt{35}}{36}, 0, \frac{251}{6}\right) & \text{air post-shock,} \\ (1, 0, 0, 1) & \text{air pre-shock,} \\ (0.138, 0, 0, 1) & \text{helium,} \end{cases} \tag{31}$$

where the shock is placed initially at $x = 0.05$. A helium bubble with initial diameter $D = 0.05$ is placed at $x = 0.1$, $y = 0.15$ within in a domain of size $[0, 0.4] \times [0, 0.3]$. Inflow and outflow conditions are applied at the left and right boundary, respectively. Neumann boundaries with zero gradient for all quantities are set at the remaining boundaries. The resolution is set to 1280×960, which resolves the helium bubble with 160 cells per diameter. The final time of the simulation is set to 0.035.

Fig. 19 shows the final density results for both HLLC and HLLC-LM. The numerical instabilities at the shock front induced by the HLLC approximation are not as dominant as for the Roe approximation [8]. Especially, no carbuncles can be observed. Instead, an odd-even decoupling develops in the backflow of the shock wave similar to the one observed for the previous example. As before, the HLLC-LM scheme produces a clean shock front without any disturbances. Moreover, the stability of the proposed scheme is tested for an extreme resolution of 1280 cells per diameter. The results shown in Fig. 20 still do not indicate any instability.

5.3. Shock interface interaction: air bubble in water in two and three dimensions

Finally, the challenging simulation of a strong 1.6 GPa shock wave in water interacting with an embedded air bubble was studied. The strong transmitted shock wave in air may suffer from the grid aligned-shock instability. First, the simulations in [8] were repeated in two dimensions with the HLLC-type solvers. Afterwards, a new fully three-dimensional simulation of the problem is presented.
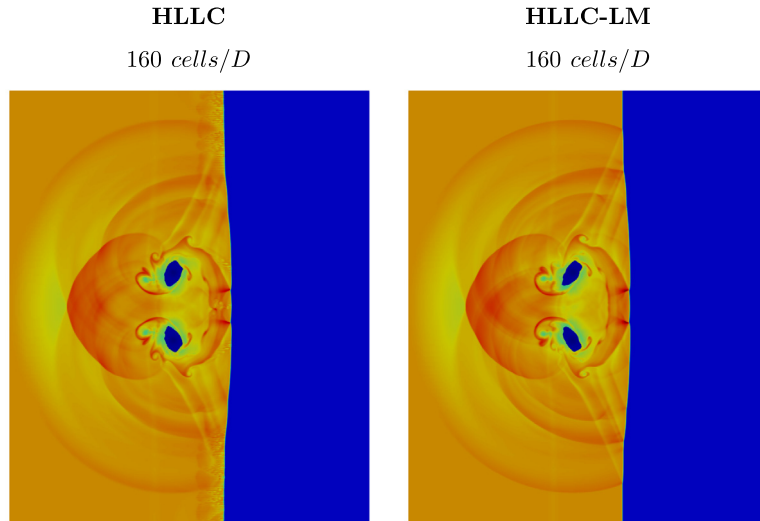
HLLC   **HLLC-LM**

160 $cells/D$ 160 $cells/D$

Fig. 19. Shock interface interaction of a helium bubble in air I: density contours from blue $= 0.138$ to red $= 7.5$ at $t = 0.035$.
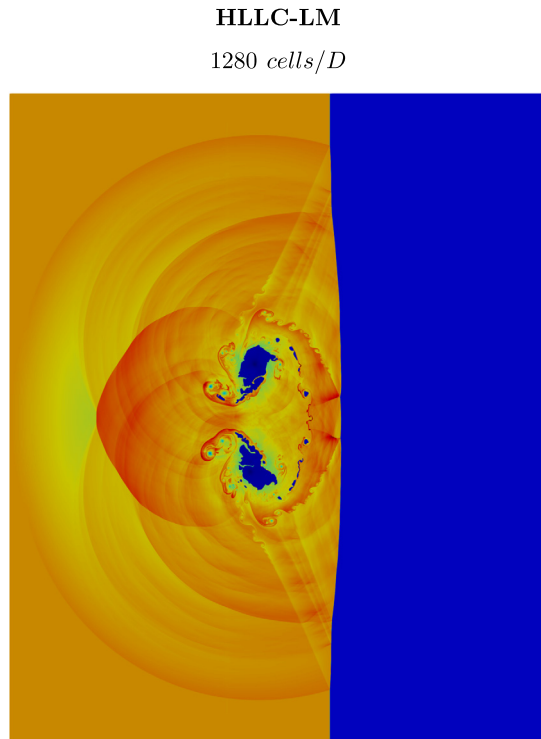
HLLC-LM

1280 $cells/D$

Fig. 20. Shock interface interaction of a helium bubble in air II: density contours from blue $= 0.138$ to red $= 7.5$ at $t = 0.035$.

The setup is chosen similar to [45] with initial states

$$(\rho, u, v, p) = \begin{cases} (1323.65, 661.81, 0, 1.6 \cdot 10^9) & \text{water post-shock} \\ (1000, 0, 0, 10^5) & \text{water pre-shock,} \\ (1, 0, 0, 10^5) & \text{air,} \end{cases} \qquad (32)$$

where water is modeled with a stiffened equation of state ($\gamma = 4.4$, $P_{\text{inf}} = 6 \cdot 10^8$) and air as ideal gas ($\gamma = 1.4$). The domain size is set to $[0, 0.024] \times [0, 0.024]$, where an air bubble with diameter $D = 0.006$ is placed in the center. The shock front is initially placed at $x = 0.008$. Inflow and outflow conditions are applied at the left and right boundary, respectively.
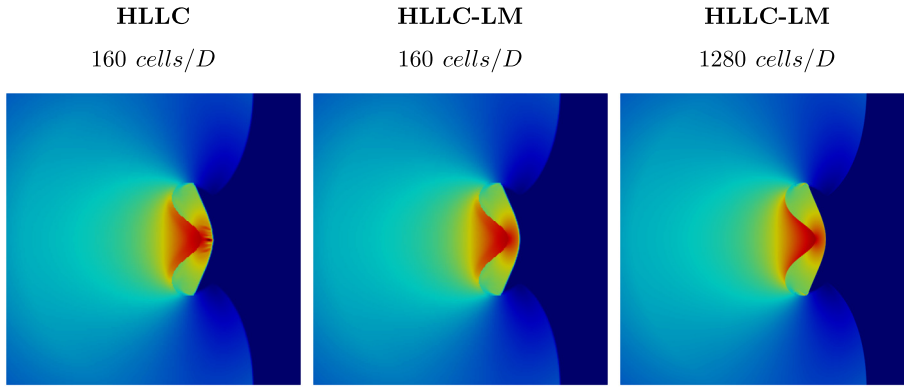
Fig. 21. Shock interface interaction of a air bubble in water at $t = 3 \cdot 10^{-6}$: velocity magnitude contours from blue $= 0$ to red $= 2850$.
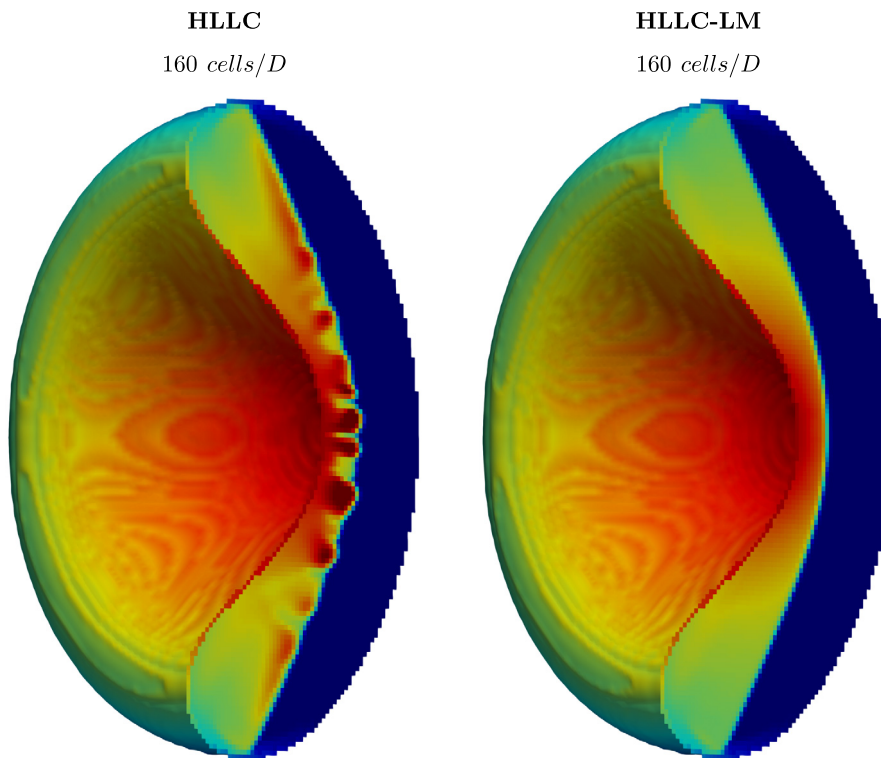

Fig. 22. 3D shock interface interaction of a air bubble in water: velocity magnitude within the air bubble from blue $= 0$ to red $= 3500$ at $t = 2.6 \cdot 10^{-6}$.

Neumann boundary condition with zero gradient for all quantities is set at the remaining boundaries. The bubble initially is resolved by 160 cells per diameter and the final time is set to $3 \cdot 10^{-6}$.

Velocity magnitude results for the HLLC and HLLC-LM solver are shown in Fig. 21. Similarly to the previous case with helium, the HLLC approximation does not create any carbuncles. However, the flow behind the shock wave in air is significantly disturbed. The HLLC-LM solver enables a stable prediction of the flow field. Again, the stability of HLLC-LM is further demonstrated by an extremely increased resolution of 1280 cells per diameter. The result of this simulation still is disturbance-free as shown in the right frame of Fig. 21.

We studied the same setup also in three dimensions with a straightforward extension of the domain in z-direction to $[0, 0.024] \times [0, 0.024] \times [0, 0.024]$. The resolution is chosen identically to the original two-dimensional case with 160 cells per diameter. Since the air bubble collapses faster in three dimensions, the final simulation time was reduced to $= 2.6 \cdot 10^{-6}$.

The results given in Fig. 22 demonstrate that the numerical instability is significantly stronger for three-dimensional simulations when the original HLLC solver is applied. Similar to the three-dimensional results for the Sedov blast wave in Section 4, now, small carbuncles can be observed, which never occurred in any of our two-dimensional simulations.

Nevertheless, the low Mach number modification in the HLLC-LM scheme leads to stable and carbuncle-free results as shown in the right frame of Fig. 22.

6. Conclusion

In this paper, the general idea that the low Mach number in transverse direction of the shock wave propagation is the reason for the grid-aligned shock instability has been exploited to design a shock-stable version of the popular HLLC approximate Riemann solver. A simple reduction of non-linear wave speeds as done for the Roe flux would lead to pure upwinding due to the one-sided definition of the HLLC flux. Therefore, a centralized formulation of the HLLC flux is proposed. Applying this centralized formulation does not only avoid the switching, but also allows for a straightforward reduction of nonlinear eigenvalues. A smooth reduction of acoustic dissipation is guaranteed using a sine function. The proposed version of the HLLC scheme with modified low Mach number behavior is denoted HLLC-LM. The modified flux *reduces the dissipation* during the flux calculation in case of low directional Mach number, and fully recovers the original HLLC flux otherwise. Thus, shock stability is retained by a *further reduction of the dissipation* of the HLLC approximation.

Results obtained with the centralized formulation have been thoroughly compared to the ones obtained with the classical formulation and found to be identical with respect to floating-point differences for all studied cases. The stability and accuracy of the HLLC-LM flux has been demonstrated for a comprehensive series of test cases commonly related to the grid-aligned shock instability. However, the prime goal of the high-order methods as applied throughout the paper is to simulate more complex flow situations than the classical carbuncle cases. The advantages of the HLLC-LM when applied to supersonic multi-component flows have been presented in detail. Stability can be maintained also for extremely high-resolved simulations. Although the HLLC flux might still be considered as suitable for most two-dimensional situations due to the fact that the occurring disturbances are commonly bounded and they rarely lead to large deviations unless resolution is drastically increased, this is not valid in three dimensions. The three-dimensional simulations presented in this paper demonstrate that the HLLC flux is likely to produce severe carbuncles similar to the Roe scheme. The HLLC-LM flux revealed excellent results also for three-dimensional simulations. Hence, the combination of HLLC-LM with state-of-the-art high-order methods allows for a robust and accurate simulation of current challenges in high-speed fluid dynamics.

CRediT authorship contribution statement

Nico Fleischmann: Conceptualization, Data curation, Investigation, Methodology, Software, Validation, Visualization, Writing - original draft. **Stefan Adami:** Project administration, Supervision, Writing - review & editing. **Nikolaus A. Adams:** Funding acquisition, Resources, Supervision, Writing - review & editing.

Declaration of competing interest

The authors declare that they have no known competing financial interests or personal relationships that could have appeared to influence the work reported in this paper.

Acknowledgements

References

[1] S.K. Godunov, A difference method for numerical calculation of discontinuous solutions of the equations of hydrodynamics, Mat. Sb. 89 (3) (1959) 271–306.
[2] P.L. Roe, Approximate Riemann solvers, parameter vectors, and difference schemes, J. Comput. Phys. 43 (2) (1981) 357–372.
[3] A. Harten, P.D. Lax, B.v. Leer, On upstream differencing and Godunov-type schemes for hyperbolic conservation laws, SIAM Rev. 25 (1) (1983) 35–61.
[4] E.F. Toro, M. Spruce, W. Speares, Restoration of the contact surface in the HLL-Riemann solver, Shock Waves 4 (1) (1994) 25–34.
[5] K. Peery, S. Imlay, Blunt-body flow simulations, in: 24th Joint Propulsion Conference, 1988, p. 2904.
[6] J.J. Quirk, A contribution to the great Riemann solver debate, in: Upwind and High-Resolution Schemes, Springer, 1997, pp. 550–569.
[7] A.V. Rodionov, Artificial viscosity in Godunov-type schemes to cure the carbuncle phenomenon, J. Comput. Phys. 345 (2017) 308–329.
[8] N. Fleischmann, S. Adami, X.Y. Hu, N.A. Adams, A low dissipation method to cure the grid-aligned shock instability, J. Comput. Phys. 401 (2020) 109004.
[9] B. Einfeldt, On Godunov-type methods for gas dynamics, SIAM J. Numer. Anal. 25 (2) (1988) 294–318.
[10] E.F. Toro, Riemann Solvers and Numerical Methods for Fluid Dynamics: A Practical Introduction, Springer Science & Business Media, 2013.
[11] E.F. Toro, The HLLC Riemann solver, Shock Waves (2019) 1–18.
[12] P. Batten, N. Clarke, C. Lambert, D.M. Causon, On the choice of wavespeeds for the HLLC Riemann solver, SIAM J. Sci. Comput. 18 (6) (1997) 1553–1570.
[13] D.S. Balsara, M. Dumbser, R. Abgrall, Multidimensional HLLC Riemann solver for unstructured meshes – with application to Euler and MHD flows, J. Comput. Phys. 261 (2014) 172–208.
[14] S. Li, An HLLC Riemann solver for magneto-hydrodynamics, J. Comput. Phys. 203 (1) (2005) 344–357.
[15] K.F. Gurski, An HLLC-type approximate Riemann solver for ideal magnetohydrodynamics, SIAM J. Sci. Comput. 25 (6) (2004) 2165–2187.

[16] X. Hu, N.A. Adams, G. Iaccarino, On the HLLC Riemann solver for interface interaction in compressible multi-fluid flow, J. Comput. Phys. 228 (17) (2009) 6572–6589.

[17] E. Johnsen, T. Colonius, Implementation of WENO schemes in compressible multicomponent flow problems, J. Comput. Phys. 219 (2) (2006) 715–732.

[18] D.P. Garrick, M. Owkes, J.D. Regele, A finite-volume HLLC-based scheme for compressible interfacial flows with surface tension, J. Comput. Phys. 339 (2017) 46–67.

[19] S.D. Kim, B.J. Lee, H.J. Lee, I.-S. Jeung, Robust HLLC Riemann solver with weighted average flux scheme for strong shock, J. Comput. Phys. 228 (20) (2009) 7634–7642.

[20] K. Huang, H. Wu, H. Yu, D. Yan, Cures for numerical shock instability in HLLC solver, Int. J. Numer. Methods Fluids 65 (9) (2011) 1026–1038.

[21] Y.-X. Ren, A robust shock-capturing scheme based on rotated Riemann solvers, Comput. Fluids 32 (10) (2003) 1379–1403.

[22] Z. Shen, W. Yan, G. Yuan, A robust HLLC-type Riemann solver for strong shock, J. Comput. Phys. 309 (2016) 185–206.

[23] W. Xie, R. Zhang, J. Lai, H. Li, An accurate and robust HLLC-type Riemann solver for the compressible Euler system at various Mach numbers, Int. J. Numer. Methods Fluids 89 (10) (2019) 430–463.

[24] S. Simon, J. Mandal, A cure for numerical shock instability in HLLC Riemann solver using antidiffusion control, Comput. Fluids 174 (2018) 144–166.

[25] S. Simon, J. Mandal, A simple cure for numerical shock instability in the HLLC Riemann solver, J. Comput. Phys. 378 (2019) 477–496.

[26] G.-S. Jiang, C.-W. Shu, Efficient implementation of weighted ENO schemes, J. Comput. Phys. 126 (1) (1996) 202–228.

[27] S. Gottlieb, C.-W. Shu, E. Tadmor, Strong stability-preserving high-order time discretization methods, SIAM Rev. 43 (1) (2001) 89–112.

[28] N. Fleischmann, S. Adami, N.A. Adams, Numerical symmetry-preserving techniques for low-dissipation shock-capturing schemes, Comput. Fluids 189 (2019) 94–107.

[29] H. Guillard, B. Nkonga, On the behaviour of upwind schemes in the low Mach number limit: a review, in: Handbook of Numerical Analysis, vol. 18, Elsevier, 2017, pp. 203–231.

[30] F. Rieper, A low-Mach number fix for Roe's approximate Riemann solver, J. Comput. Phys. 230 (13) (2011) 5263–5287.

[31] X.-s. Li, C.-w. Gu, An all-speed Roe-type scheme and its asymptotic analysis of low Mach number behaviour, J. Comput. Phys. 227 (10) (2008) 5144–5159.

[32] H. Guillard, C. Viozat, On the behaviour of upwind schemes in the low Mach number limit, Comput. Fluids 28 (1) (1999) 63–86.

[33] H. Guillard, A. Murrone, On the behavior of upwind schemes in the low Mach number limit: II. Godunov type schemes, Comput. Fluids 33 (4) (2004) 655–675.

[34] Z. Chen, X. Huang, Y.-X. Ren, Z. Xie, M. Zhou, Mechanism study of shock instability in Riemann-solver-based shock-capturing scheme, AIAA J. 56 (9) (2018) 3636–3651.

[35] A. Harten, Adaptive multiresolution schemes for shock computations, J. Comput. Phys. 115 (2) (1994) 319–338.

[36] J.W. Kaiser, N. Hoppe, S. Adami, N.A. Adams, An adaptive local time-stepping scheme for multiresolution simulations of hyperbolic conservation laws, J. Comput. Phys. X 4 (2019) 100038.

[37] X.Y. Hu, N.A. Adams, C.-W. Shu, Positivity-preserving method for high-order conservative schemes solving compressible Euler equations, J. Comput. Phys. 242 (2013) 169–180.

[38] F. Kemm, Heuristical and numerical considerations for the carbuncle phenomenon, Appl. Math. Comput. 320 (2018) 596–613.

[39] P. Woodward, P. Colella, The numerical simulation of two-dimensional fluid flow with strong shocks, J. Comput. Phys. 54 (1) (1984) 115–173.

[40] F. Kemm, On the proper setup of the double Mach reflection as a test case for the resolution of gas dynamics codes, Comput. Fluids 132 (2016) 72–75.

[41] X.Y. Hu, B. Khoo, N.A. Adams, F. Huang, A conservative interface method for compressible flows, J. Comput. Phys. 219 (2) (2006) 553–578.

[42] L. Fu, A low-dissipation finite-volume method based on a new TENO shock-capturing scheme, Comput. Phys. Commun. 235 (2019) 25–39.

[43] E.J. Tasker, R. Brunino, N.L. Mitchell, D. Michielsen, S. Hopton, F.R. Pearce, G.L. Bryan, T. Theuns, A test suite for quantitative comparison of hydrodynamic codes in astrophysics, Mon. Not. R. Astron. Soc. 390 (3) (2008) 1267–1281.

[44] I. Glass, J. Kaca, D. Zhang, H. Glaz, J. Bell, J. Trangenstein, J. Collins, Diffraction of planar shock waves over half-diamond and semicircular cylinders: an experimental and numerical comparison, in: AIP Conference Proceedings, vol. 208, AIP, 1990, pp. 246–251.

[45] O. Haimovich, S.H. Frankel, Numerical simulations of compressible multicomponent and multiphase flow using a high-order targeted ENO (TENO) finite-volume method, Comput. Fluids 146 (2017) 105–116.